Microstructure, ionic conductivity and mechanical properties of tape-cast $Li_{1.5}Al_{0.5}Ti_{1.5}P_3O_{12}$ electrolyte sheets

Enkhtsetseg Dashjav*[1], Michael Gellert[3], Gang Yan[1], Daniel Grüner[1], Nico Kaiser[4], Stefan Spannenberger[4], Irina Kraleva[5], Raul Bermejo[5], Marie-Theres Gerhards[1], Qianli Ma[1], Jürgen Malzbender[1], Bernhard Roling[4] Frank Tietz[1,2], Olivier Guillon[1,2,6]

[1]Forschungszentrum Jülich GmbH, Institute of Energy and Climate Research, 52425 Jülich, Germany

[2] Forschungszentrum Jülich GmbH, Helmholtz-Institute Münster, 52425 Jülich, Germany

[3] GNB Industrial Power Exide Technologies GmbH, Im Thiergarten, 63654 Büdingen, Germany

[4]Philipps-Universität Marburg, Fachbereich Chemie and Wissenschaftliches Zentrum für Materialwissenschaften (WZMW), Hans-Meerwein-Strasse 4, 35043 Marburg, Germany

[5] Montanuniversität Leoben, Institut für Struktur- und Funktionskeramik, Franz Josef-Straße 18, A-8700 Leoben, Austria

[6]Jülich Aachen Research Alliance, JARA ENERGY

**E-mail: e.dashjav@fz-juelich.de, tel.: +49 2461 61-96769, fax.: +49 2461 61-5700*

Abstract

Free-standing $Li_{1.5}Al_{0.5}Ti_{1.5}P_3O_{12}$ electrolyte sheets with a thickness of 50–150 µm were prepared by tape casting followed by sintering at 850–1000 °C in air. While a sintering temperature of 850 °C was too low to achieve appreciable densification and grain growth, a peak relative density of 95 % was obtained at 920 °C. At higher sintering temperatures, the microstructure changed from a bimodal grain size distribution towards exclusively large grains (> 10 µm), accompanied by a decrease in relative density (down to 86 % at 1000 °C). In contrast, ionic conductivity increased with increasing sintering temperature, from 0.1 mS/cm at 920 °C to 0.3 mS/cm at 1000 °C. Sintering behavior was improved by adding 1.5 % of amorphous silica to the slurry. In this way, almost full densification (99.8 %) and an ionic conductivity of 0.2 mS/cm was achieved at 920 °C.

Mechanical characterization was carried out on the almost fully densified material, yielding elastic modulus and hardness values of 109 and 8.7 GPa, respectively. The fracture strength and Weibull modulus were also characterized. The results confirm that densification and reduction of grain size improve the mechanical properties.

Keywords: LATP, NaSICON, solid electrolyte, tape casting, grain boundaries, sintering, mechanical properties

Introduction

The increasing interest in batteries with solid electrolytes has led to the development of many new fast ion conductors in recent years, for example Li^+-conducting sulphides [1, 2], thiophosphates [3, 4, 5], argyrodites [6, 7, 8], Na^+-conducting thiophosphates [9, 10], and NaSICONs [11, 12], to mention just a few. Among the oxides and phosphates, however, there are still only three types of solid electrolytes with similar fast ion conduction: the family of NaSICON-type materials [13,14], the perovskites [15, 16], and the wide variety of garnet materials [17,18]. Among the group of NaSICON-type materials, the highest ionic conductivity of up to 5 mS cm^{-1} has been reported for $Li_{1.5}Al_{0.5}Ge_{1.5}P_3O_{12}$ [19, 20], but its wider application can be ruled out due to its usage of the very expensive raw material germanium. Typically, conductivity values have been obtained on the basis of pressed and sintered thick pellets, which is the simplest way to produce ceramic bodies. As soon as more sophisticated processing techniques become involved – for example in studies on shaping and engineering the ceramic sheets, layers, or tubes – only a limited number of studies have been published. In many cases, it has not been possible to reproduce high conductivity values for thin sheets or more complex structured bodies [19, 21, 22], often due to the lower density of the fabricated components. In the case of NaSICON-type materials, only a few reports on ceramic processing are available. Tape casting has been used more frequently [19, 22,23,24,25,26, 27] than other fabrication techniques such as extrusion [28] or aerosol deposition [29]. The present study discusses the preparation and characterization of tape-cast $Li_{1.5}Al_{0.5}Ti_{1.5}(PO_4)_3$ (LATP) sheets. A comparison of tape-cast Li-NaSICON materials is provided in Table 1.

Table 1: Comparison of room temperature conductivities of tape-cast Li-NaSICON layers

	σ_{total} / mS cm^{-1}	Layer thickness / µm	Ref.
$Li_{1.3}Al_{0.3}Ti_{1.7}P_3O_{12}$	0.06	20	[23]
$Li_{1.7}Al_{0.3}Ti_{1.7}Si_{0.4}P_{2.6}O_{12}$ + 5 wt.% Li excess	0.43	52	[21]
$Li_{1.3}Al_{0.3}Ti_{1.7}P_3O_{12}$ + 0.5 mol% $AlPO_4$	0.18	40	[24]
$Li_{1.4}Al_{0.4}Ge_{1.6}P_3O_{12}$	0.34	75	[25]
$Li_{1.4}Al_{0.4}Ge_{1.6}P_3O_{12}$ +5 wt.% TiO_2	0.84	200	[26]
$Li_{1.5}Al_{0.5}Ge_{1.5}P_3O_{12}$	0.64	200	[19]

In addition to high ionic conductivity, the mechanical properties of solid electrolytes must facilitate reliable handling of the components and safe operation under application-relevant conditions, for instance applying pressure to the cell stack. This requires characterization of the following aspects: elastic modulus (E), which couples induced strains and failure-relevant stresses; hardness (H); as a limit of plasticity, strength as a measure of sustainable strains and crack growth resistance (K_R); as a measure of the crack growth resistance. Particularly, Monroe and Newman [30] notably emphasized the importance of the elastic properties of materials to be used in batteries. According to their work, in order to prevent the formation of dendrites at the Li electrode/solid electrolyte interface during cycling, the shear modulus of the solid electrolyte should be more than twice the shear modulus of Li metal (4.25 GPa). Based on the literature, it appears that the elastic modulus of LATP is sufficient to satisfy these boundary conditions, being in the range of 81-115 GPa; the hardness of LATP is around 7.8 GPa and the crack growth resistance around 1 $MPa \cdot m^{1/2}$ [31-33]. Nevertheless, more recent studies suggest that elastic properties alone are not sufficient as a selection guideline; crack growth resistance must also be considered [34-37]. For brittle materials that possess an inherent scatter in fracture stresses, a fracture-based reliability analysis is of paramount importance, since safety factors are the most uncertain aspect of a designs for these materials [38, 39]. In real application, the electrolyte experiences stress and comes into contact with other materials. The probability distribution of structural strength and lifetime is known to follow a Weibull distribution, determining the time or load related to a tolerable failure probability [40]. Since porosity has a significant impact on the mechanical behavior of a material [41, 42], the mechanical properties of the densest material is chosen in this work for the mechanical assessment.

For this study, free-standing $Li_{1.5}Al_{0.5}Ti_{1.5}P_3O_{12}$ electrolyte sheets with a thickness of 50-150 µm were produced using a tape casting method followed by sintering at different temperatures. The composition, microstructure, ionic conductivity and mechanical properties of the LATP sheets were investigated.

Experimental

The LATP powder was prepared by means of a solution-assisted solid state reaction, as described elsewhere [43] and was calcined at 750 °C. After calcination, the powder was ball-milled in ethanol with ZrO_2 balls for 24 h, then dried at 80 °C for another 24 h and subsequently mortared to obtain the fine-grained quality required for further use. The particle size (0.7 µm average) and surface area (15.23 $m^2 g^{-1}$) were determined by means

of dynamic light scattering and the Brunauer–Emmett–Teller (BET) method, respectively. For the preparation of electrolyte sheets by tape casting, the LATP powder was dispersed in a mixture of ethanol, methylethylketone, polyvinylbutyral (Butvar B-98), Nousperse FX9086 (Elementis Specialties), polyethylene glycol (PEG400), and Solusolv S-2075 (Solutia Inc.). For electrolyte sheets with sintering additives, 1.5 % of an amorphous SiO_2 nano-powder (Alfa Aesar) was added to the mixture, hereafter abbreviated as LATP:Si. The homogenized dispersions were degassed at 20 kPa for 10 minutes and then cast using a tape-casting machine (KARO Cast 300-7 from KMS, Automation GmbH, Germany) with a slit height of 150 – 400 µm and a drawing speed of 3 mm/s. The cast foils were dried and cut into circular discs that were sintered in air at temperatures of 850 – 1000 °C for 1 h on a quarzglas substrate, resulting in 50 – 150 µm thick sheets. For the sintering the samples were heated up to 500 °C with slow heating rate of 1 K/min and then up to and sintering temperature T_s (850 – 1000 °C) with heating rate of 5 K/min in air under normal pressure of 1 bar. While different dwell time between 1h and 6h did not change the density and shrinkage of the disks, we decided to use 1 h for sintering time. The sintering temperature and corresponding density together with ionic conductivity of the disk are summarized in Table 3.

The tape-cast sheets were analyzed using thermogravimetry (TG) and differential scanning calorimetry (DSC) with a heating rate of 300 K/h. A Netzsch STA 449F1 differential thermal analyzer, coupled with a mass spectrometer, was used to obtain measurements. The DSC and TG measurements were performed in ambient air. Volatile species were continuously detected by the mass spectrometer during the measurement process.

The sintered disks were analyzed by means of X-ray diffraction analysis (XRD) using a D4 ENDEAVOR (Bruker AXS) with Cu-K_α radiation. The density was determined using the Archimedes method. A Zeiss SUPRA 50 VP scanning electron microscope was used to perform scanning electron microscopy (SEM) investigations. For the purposes of microstructural characterization, the fracture surfaces of freshly broken discs were sputter-coated with a thin layer of iridium. For the AC impedance measurements, platinum electrodes were sputtered on both faces of the disks. The samples were then placed in a two-electrode high-voltage sample cell (Novocontrol, BDS 1200, Hundsangen, Germany). AC impedance data were collected using a Novocontrol Alpha-AK impedance analyzer. The analyzer was connected to a ZG2 test interface (Novocontrol). The measurements were carried out in temperature range of -120 °C to 100 °C, controlled by a Quatro Cryosystem (Novocontrol).

For the purposes of indentation testing, a LATP:Si pellet was embedded in water-free epoxy resin and polished to derive *E, H,* and K_R. The specimen was polished with 400 to 4000 grit sandpaper and water-free polyethylene glycol (PEG) polishing suspensions with 0.2 μm SiO_2. A water-free polishing system was adopted to prevent proton/lithium exchange due to water absorption; therefore, this was not expected to have a significant impact on the mechanical properties. Indentation testing is a commonly used method for determining the mechanical properties of ceramic materials, particularly in energy-related applications [44–46]. Indentation experiments were carried out here using a Fischer instrument (Fischerscope H100 Micro Tester) with a Vickers tip. To obtain the intrinsic *E* and *H* values of the LATP:Si, different loads were applied ranging from 30 to 500 mN. At each load, 10 indentations were performed to obtain a representative average and deviation. The holding period was 1 s and the acquisition rate was 10 Hz. *E* and *H* were evaluated from the indentation load–displacement curve according to the Oliver–Pharr method [47]. A value of 0.25 was used for Poisson's ratio of LATP:Si [48].

Crack growth resistance values were determined by means of the conventional Vickers indentation method [49] using a microhardness tester (Micromet 1, Buehler Ltd.). Crack lengths induced by the Vickers indentation imprint were measured via an optical microscope immediately after indentation to avoid subcritical crack growth effects. Loads of 3 N and 5 N were applied to induce cracks with sufficient length for toughness calculation. For each load, at least 5 indentations were employed. Crack growth resistance is determined by measuring the lengths of cracks emanating from the corners of indentations at a given load, where the model for the K_R calculation is dependent on the crack type [50]. In this study, the ratio of measured crack length (l) to indentation imprint half-diagonal (a) matched with the median crack model ($c/a \geq 2.25$, where $c = a + l$), and therefore the Anstis equation was adopted [51]:

$$K_R = 0.016 \left(\frac{E}{H}\right)^{1/2} \cdot \frac{P}{(a+l)^{3/2}} \qquad (1)$$

where P is the load.

The biaxial bending strength of LATP:Si pellets was investigated via the ball-on-three-balls (B3B) test. In the B3B test, a rectangular plate (or disc) is symmetrically supported by three balls at one plane and loaded by a fourth ball in the center of the opposite plane. More details about the test can be found elsewhere [52, 53]. In the present case, all four balls had a diameter of 5 mm and 13 specimens were cut into 6.6 × 7.1 × 0.2 mm^3

rectangular plates for the test. A pre-load of 1 N was applied to hold the specimen between the four balls. The tests were then conducted under displacement control at a rate of 0.01 mm/min and at room temperature, using a universal testing machine (Zwick Z010, Zwick/Roell, Ulm, Germany) with a load cell of 200 N. The load was increased until fracturing occurred and the fracture load was used to calculate the maximum tensile biaxial stress in the specimen at the moment of fracture; see [52, 53]. To characterize the reliability of the ceramic materials, the probability of failure P_f of the ceramic materials was analyzed using a two-parameter Weibull distribution [54]:

$$P_{\mathrm{f}} = 1 - \exp\left[-\left(\frac{\sigma}{\sigma_0}\right)^m\right] \tag{2}$$

In the equation, σ_0 is the characteristic strength, i.e. the stress for which the survival probability is 0.37; and m is the Weibull modulus, which indicates how rapidly the stress changes with probability, i.e. the variability of the fracture stresses.

Results and Discussion

Sintering conditions, thermal stability, and microstructure

The green tapes were analyzed by means of DSC and TG analysis to identify the crystallization temperature and mass loss related to removal of the organic compounds. A representative DSC/TG measurement of LATP and LATP:Si tapes is shown in Figure 1. Organic additives were removed in two major processes. According to the data collected from the mass spectrometer, the both DSC signals at 273 °C and 319.6 °C, as well as mass loss between 180°C and 300 °C were related to the pyrolysis of the polyvinylbutyral resin. Various organic molecules such as propylene, ethylene, carbon dioxide, and water were detected by means of mass spectrometry. Residual carbon was then removed between 350 °C and 500 °C, where only carbon and carbon dioxide signals were observed in the mass spectrum. A distinct signal recorded at 783 °C was most likely related to the crystallization of LATP [55].

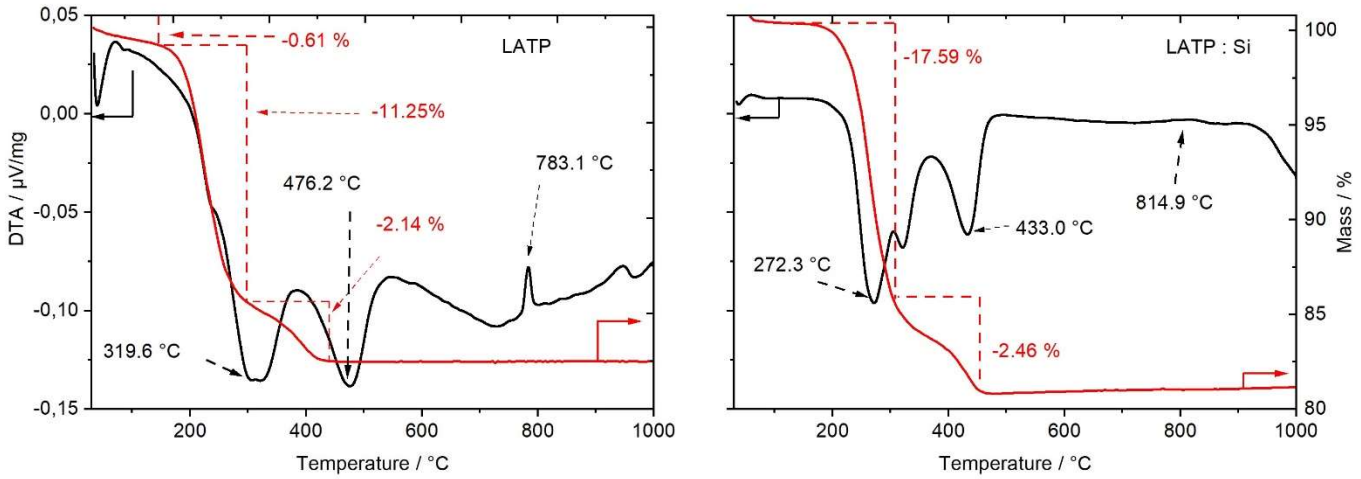

Figure 1: DSC/TG measurement of (a) LATP and (b) LATP:Si green tapes. The heating rate was 5 K/min up to 1000 °C. The indicated temperatures refer to multi-step combustion processes of organic additives and crystallization at higher temperatures.

The tapes were then sintered at various temperatures from 850 °C to 1000 °C to identify optimal conditions for densification. After sintering, the XRD patterns were recorded to detect secondary phases, which are common in LATP-type ceramics [55] (see Figure 2). All samples show a rhombohedral structure (space group $R\bar{3}c$) of LATP as the main phase. Tapes sintered in the temperature range of 850-920 °C contain small amounts (< 5 vol. %) of $AlPO_4$ as a secondary phase, whereas tapes sintered at 970°C and above are almost single phase. Relative densities of more than 90 % were achieved for most sintering temperatures. The highest density (95.3 %) was achieved for a sintering temperature of 920 °C. Above that temperature the density decreased rapidly to 86.7 % at 1000 °C. Figure 3 shows SEM micrographs of the fracture surfaces of the sintered tapes. All samples show closed porosity. Tapes sintered at 900 °C and below consist of a mixture of larger grains (> 2 µm) and very small grains (< 0.5 µm), whereas specimens sintered at 950 °C and higher temperatures consist solely of much larger grains (> 10 µm). The onset of the transition from normal sintering behavior to abnormal grain growth is at temperatures of around 920 °C, where a portion of the small grains is retained.

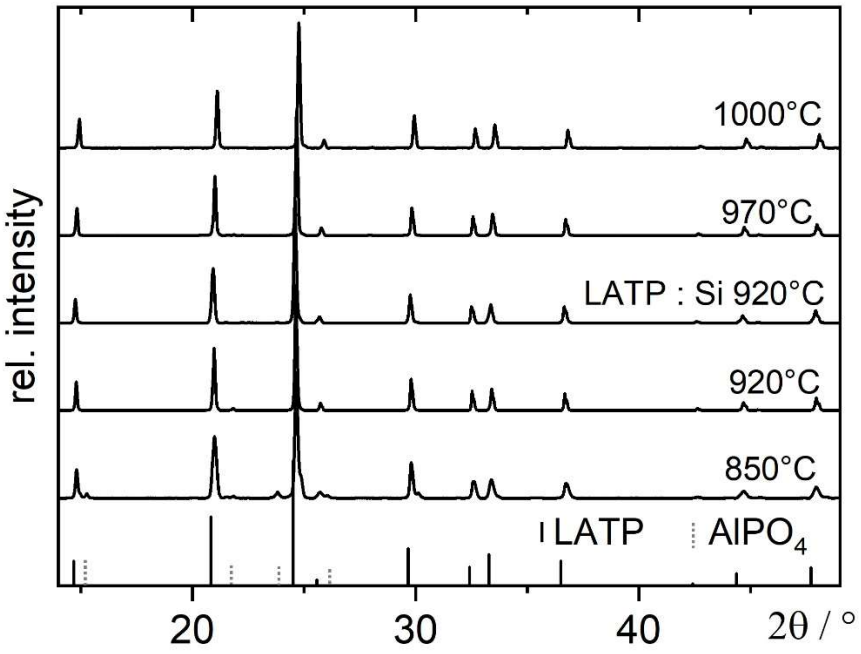

Figure 2: XRD patterns of LATP sheets sintered at different temperatures.

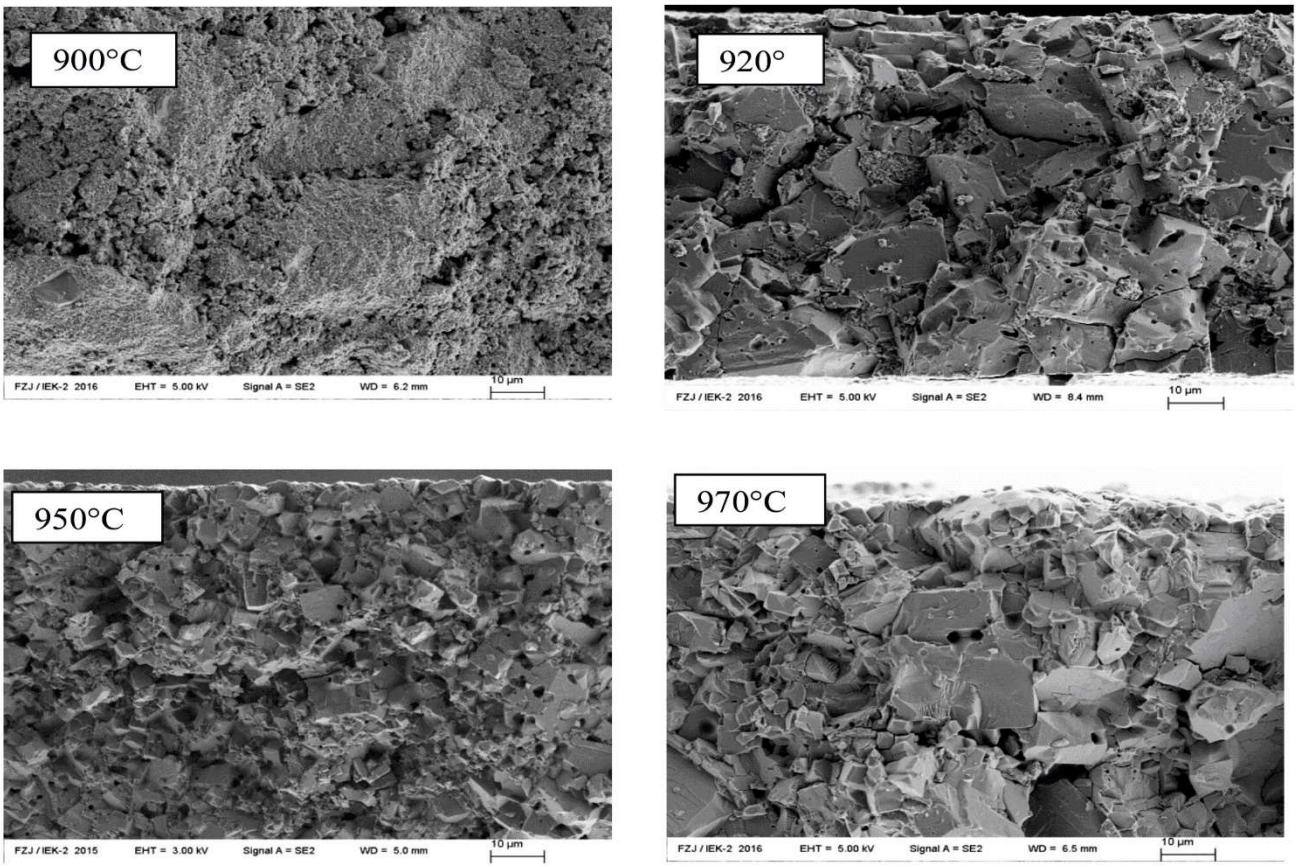

Figure 3: SEM images of the fracture surface of LATP sintered at different temperatures.

Several reports [56-58] have indicated that the densification of LATP can be enhanced by using glass forming additives such as SiO_2. Consequently, a small amount of amorphous SiO_2 powder was added to the slurry. In fact, the results of the DSC/TG measurement for this LATP:Si tape were very similar to those for the unmodified LATP (see Figure 1). A multi-step combustion process took place in the temperature range between 200 °C and 450 °C. Instead of a distinct process, where the crystal structure formation causes a peak in the DSC curve, a small and broad endothermic feature appeared at about 815 °C, which is slightly higher than the crystallization temperature observed for the unmodified LATP. To compare the densification of the unmodified LATP with that of the LATP:Si, the sintering temperature that yielded the highest density for LATP (920 °C) was used for thermal treatment. In contrast to the unmodified LATP, no secondary phase was detected for LATP:Si at the sintering temperature of 920 °C in the XRD pattern (see Figure 2).

Density measurements revealed a significant increase in theoretical density to 99.8 %. This can be associated with a mixture of interconnected large grains (> 4 µm) and very small grains that fill up interstitial spaces, as shown in the SEM micrograph in Figure 4. The microstructure is very similar to the one of the pure LATP sheet sintered at the same conditions. The sintering temperature of 920 °C marks the onset of abnormal grain growth, which appears to be delayed by the presence of silica: between the large grains exist more fine particles. Handling of the LATP:Si samples had already indicated an enhanced mechanical stability before the mechanical properties were determined.

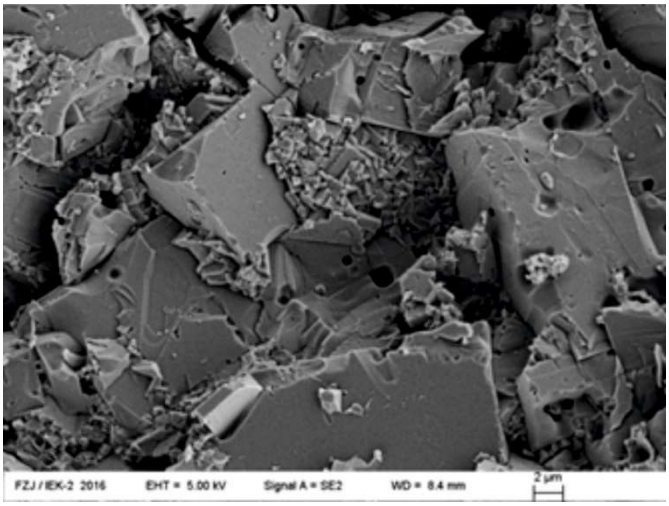

Figure 4: SEM micrograph of the fracture surface of LATP:Si sintered at 920 °C.

Electrical conductivity

The Nyquist diagrams of the complex impedance of LATP sintered at 920°C are presented for different temperatures in Figures 5a and 5b. In general, they consist of three different elements: two semicircles that represent the grain and grain boundary conduction processes, followed by a capacitive process associated with electrode polarization [59]. The grain semicircle recorded and clearly visible at a tempareature of -120 °C is shown in Figure 5b. The impedance spectra were fitted using an equivalent circuit shown in Figure 5c. This circuit contained a parallel combination of resistance R_B, and a constant-phase element CPE_B describing the bulk ion transport in the grains. The grain boundary properties are represented by a parallel combination of a resistance R_{GB} and a constant-phase element CPE_{GB}. Finally, a constant-phase element CPE_{EL} related to the electrode polarization. A contribution of parallel grain-boundary conduction was neglected due to the large average grain size (» 200 nm). The impedance of the constant-phase element was given as $Z_{CPE} = \frac{1}{Q} \cdot (i\omega)^{-n}$ with $n \leq 1$. Effective capacitances were extracted using $C_{eff} = Q^{1/n} R^{(1-n)/n}$ [60], where R is the resistance in parallel.

The bulk semicircle could be clearly distinguished from the grain boundary semicircle at temperatures below -20 °C. The determined capacitancies of the bulk conduction process were in the range of $4 \cdot 10^{-10}$ F cm^{-2}, whereas the grain boundary capacitancies were much larger ($2 \cdot 10^{-8}$ F cm^{-2}). The total resistance was dominated by grain boundary processes, that were almost two orders of magnitude more resistive than the bulk process, leading to a total ionic conductivity of 0.1 mS/cm at 20 °C. For comparison, a bulk conductivity of about 3 mS/cm was obtained at 20 °C, which is in very good agreement with measurements on single crystals [55] and other polycrystalline specimens [61-64]. The resulting Arrhenius plot of the bulk and total conductivity (here equivalent to the grain boundary conductivity) is shown in Figure 6.

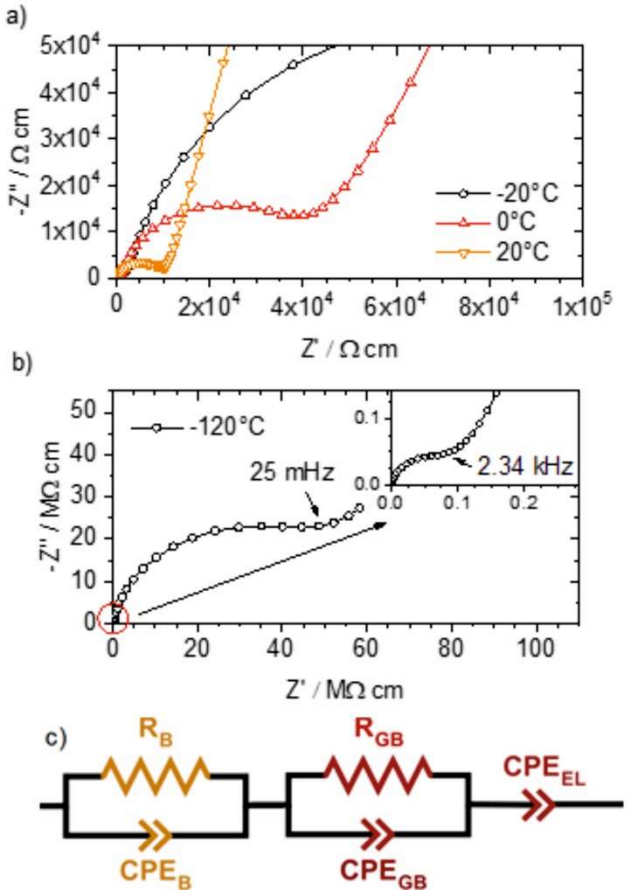

Figure 5: (a) Nyquist plots of LATP thick films sintered at 920 °C recorded at different temperatures. (b) At a temperature of -120 °C, the contribution of bulk material and grain boundaries can be distinguished. (c) Equivalent circuit used for the impedance analysis.

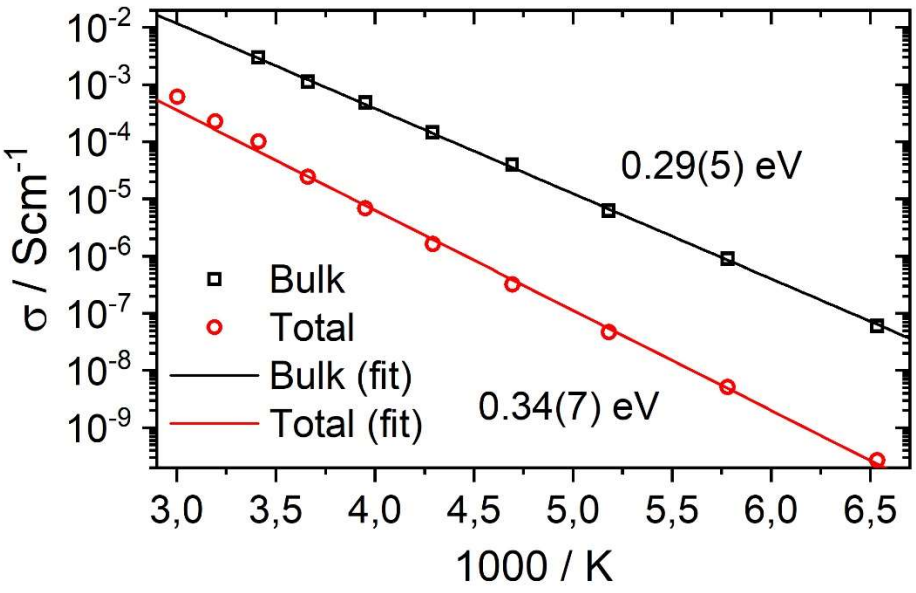

Figure 6: Arrhenius plot of the bulk and total conductivity of LATP (100 µm) sintered at 920 °C.

The activation energy of the grain boundary processes was approximately 350 meV, while the bulk activation energy was even lower than 300 meV. These results are in excellent agreement with a previous studies based on pressed pellets [13, 65].

A typical Nyquist plot of the complex impedance of LATP:Si is shown in Figure 7. Again, grain boundary and bulk processes could be clearly separated, but only up to temperatures of -100 °C. At higher temperatures the grain boundary process could not be separated from the bulk resistance, with the results that only the total conductivity could be extracted. Despite this, the capacitance of the bulk and grain boundary process remained unchanged compared to unmodified LATP.

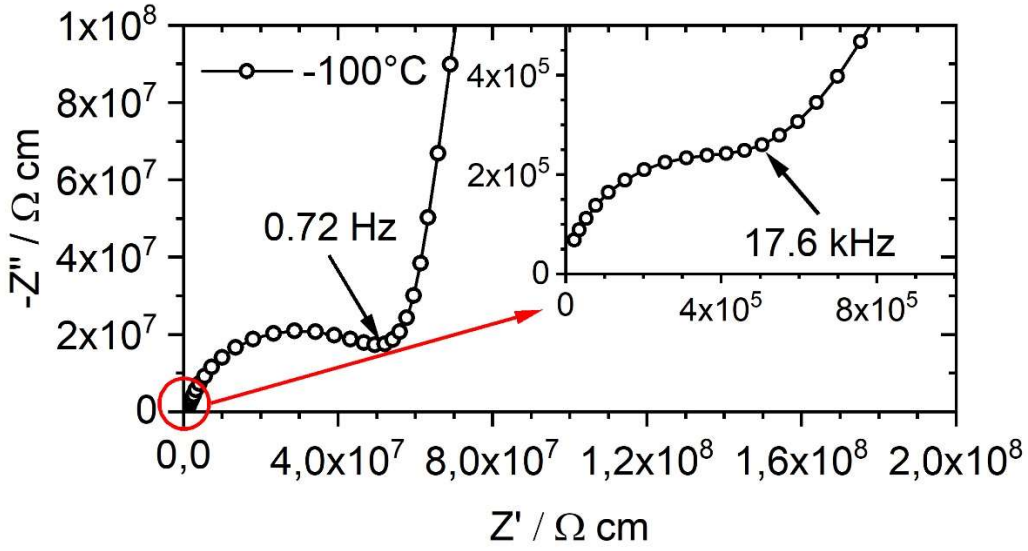

Figure 7: Nyquist diagram of LATP:Si tape sintered at 920 °C recorded at -100 °C.

The resulting Arrhenius plot is presented in Figure 8. The activation energy of the total conductivity was very similar to that in the unmodified LATP tape, whereas the conductivity value doubled to yield 0.2 mS/cm at 20 °C. This is most likely a consequence of the increased density [64].

In the case of the bulk properties, both the activation energy and the conductivity are reduced. While the activation energy decreased to 260 meV, the bulk conductivity at 20 °C dropped from 3 mS/cm for LATP to 1.2 mS/cm for LATP:Si (extrapolated).

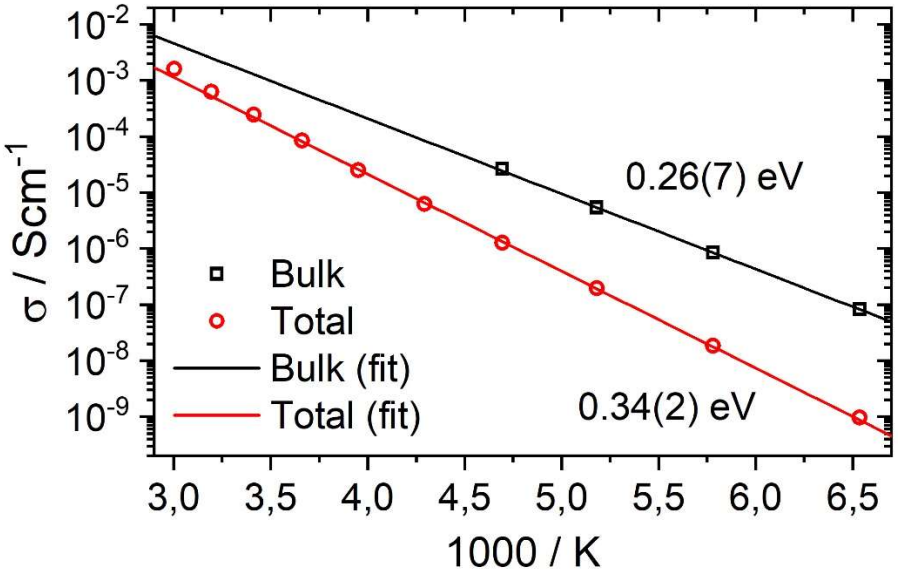

Figure 8: Arrhenius plot of the bulk and total conductivity of LATP:Si (100 µm) tape sintered at 920 °C.

Mechanical properties

Since porosity can affect the mechanical behavior of ceramic materials [41, 42], the LATP:Si with the highest density was chosen for the investigation of mechanical properties.. The commonly used indentation method was used to test the LATP:Si for hardness, elastic modulus, and crack growth resistance, where the maximum applied load was 500 mN (penetration depth ~ 3 µm). Hence, since the pellet thickness was approximately 1 mm, any influence on the results due to the compliant embedding material can be ruled out.

Figure 9 presents the elastic modulus (*E*) and hardness (*H*) of the LATP:Si as a function of load. It can be seen that both values decreased with increasing load. The impact of grain boundaries on the mechanical properties increased due to the wider load-carrying zone, which appeared to decrease the apparent properties of the material [66]. In addition, the bimodal grain size can also enhance the load dependence of mechanical properties, as small grains induce more grain boundaries. By virtue of the low porosity, any effects resulting from voids appeared to be negligible. The *E* and *H* values at low load represent the intrinsic property of the LATP:Si, whereas the values at higher load indicate the polycrystalline property. The average elastic modulus and hardness at low load were 109 ± 5 GPa and 8.7 ± 0.4 GPa, respectively. Literature values for the elastic modulus of LATP are in the range of 81–115 GPa [30, 32] for a hardness of 7.1 ± 0.4 GPa [31]. The elastic modulus and hardness of LATP:Si as determined here appear to be slightly higher than the values reported by Jackman and Cutler [31]. The sample investigated here had a density of 99.8%, with small grains filling the

interstitial space of large grains, whereas the reported density of LATP was 97.0% [31] with grain sizes of around 30 μm. Additionally, in Jackman and Cutler's study [31], the elastic modulus was measured via a ring-on-ring test machine where the effectively deformed zone was far larger than the indentation test adopted here. As the above results demonstrate, the larger the load-carrying zone, the lower the *E* and *H* values obtained.

Vickers indentations were utilized in the current study to determine the crack growth resistance of LATP:Si at different loads. It was found that below 1 N no obvious cracks could be generated, while above 10 N, the sample surface was crushed. Hence, the crack growth resistanceof LATP:Si was tested at 3 N and 5 N. Since the ratio of the crack length (l) to half-diagonal (a) of the imprints met with the condition ($l/a \geq 1.25$) of median (half-penny) cracks, the equation (1) was adopted [51]. The crack growth resistancevalues of LATP:Si derived for loads of 3 N and 5 N were 1.1 ± 0.3 and 1.2 ± 0.3 MPa·m$^{1/2}$, respectively, were therefore independent of the applied load. Jackman and Cutler [31] reported that the crack growth resistanceof LATP material determined by the single edge notch bending method was 1.1 ± 0.3 MPa·m$^{1/2}$, which is in very good agreement with that of LATP:Si characterized here. Furthermore, for comparison, the crack growth resistanceof the garnet-type electrolyte $Li_7La_3Zr_2O_{12}$ is in the range of 0.9 -1.25 MPa·m$^{1/2}$ [67, 68] and the corresponding value range for the perovskite-type electrolyte $Li_{0.33}La_{0.57}TiO_3$ is 1.15–1.24 MPa·m$^{1/2}$ [69, 70], which reveals that LATP:Si has a similar crack growth resistanceto other potential solid electrolytes .

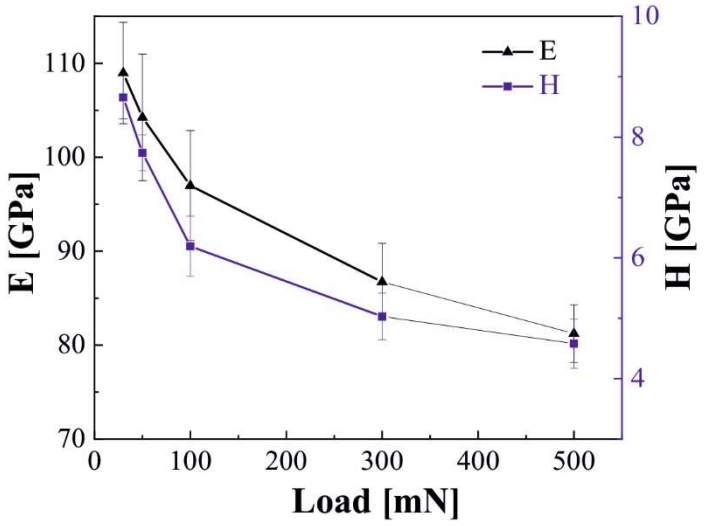

Figure 9: Elastic modulus and hardness of LATP:Si as a function of indentation load.

In order to gain insight into fracture stresses and reliability of the samples, ball-on-three-ball B3B bending tests were carried out at room temperature [53]. The fracture stress data derived were described by means of

a 2-parameter Weibull distribution yielding the characteristic strength and Weibull modulus [54]. Industry standards suggest a minimum of 30 specimens as a basis for a Weibull statistical analysis [71]. However, due to limited availability of materials (13 samples), it was not possible to test such a large number of specimens here. Therefore, although the data were indeed analyzed using Weibull statistics, the result should only be considered as a tentative indication of material behavior.

As illustrated in Figure 10, the Weibull parameters were calculated via linear fitting with 90% confidence intervals as σ_0 = 168 [160.7 – 175.3] MPa and m = 12.8 [7.8 – 16.8]. The effective volume of LATP:Si was calculated using online software (http://www.isfk.at/de/960/) as 0.265 mm^3. The mechanical properties of LATP:Si, as summarized in Table 2 are slightly favorable those of LATP reported by Jackman and Cutler [31], according to which the characteristic strength of high-purity, fine-grained (HPFG) LATP is 130 MPa and the Weibull modulus is 8. Since the Weibull theory predicts a size effect on strength, i.e. that strength decreases with increasing effective volume, the fracture strength of LATP:Si can be regarded to be the same as that of LATP [71]. It can be seen that the Weibull modulus of LATP:Si is in a similar range as for other ceramic materials, i.e. 5 to 20 [72]. Compared with the ceramic materials $LiNbO_3$ and $LiTaO_3$, which were tested with the same B3B test method by Gruber [73], the Weibull modulus of LATP:Si is higher than that of $LiNbO_3$ (3.8–6.9) and $LiTaO_3$ (3.4–6.3), although the limited number of specimens and the confidence interval mean that further tests are required to enable a final conclusion. However, the characteristic strength of LATP:Si is lower than that of $LiNbO_3$ (638–2036 MPa) and $LiTaO_3$ (669–1802 MPa). It can be assumed that the fracture reliability of the solid electrolyte LATP:Si (with a size of 6.6 × 7.1 × 0.2 mm^3) is superior to that of the cathode materials $LiNbO_3$ and $LiTaO_3$, even though the fracture strength is lower. The Weibull statistics for LATP:Si presented here can be used as a reference for further LATP material design and as a comparison in probabilistic maximum stress calculations for component simulations.

Table 2. Mechanical properties of LATP:Si material. Numbers in brackets indicate the 90 % confidence interval.

E (GPa) at 30 mN	H (GPa) at 30 mN	K_R (MPa·m$^{1/2}$) at 3 N	m	σ_0 (MPa)
109 ± 5	8.7 ± 0.4	1.1 ± 0.3	12.8 [7.8 – 16.8]	168 [160.7 – 175.3]

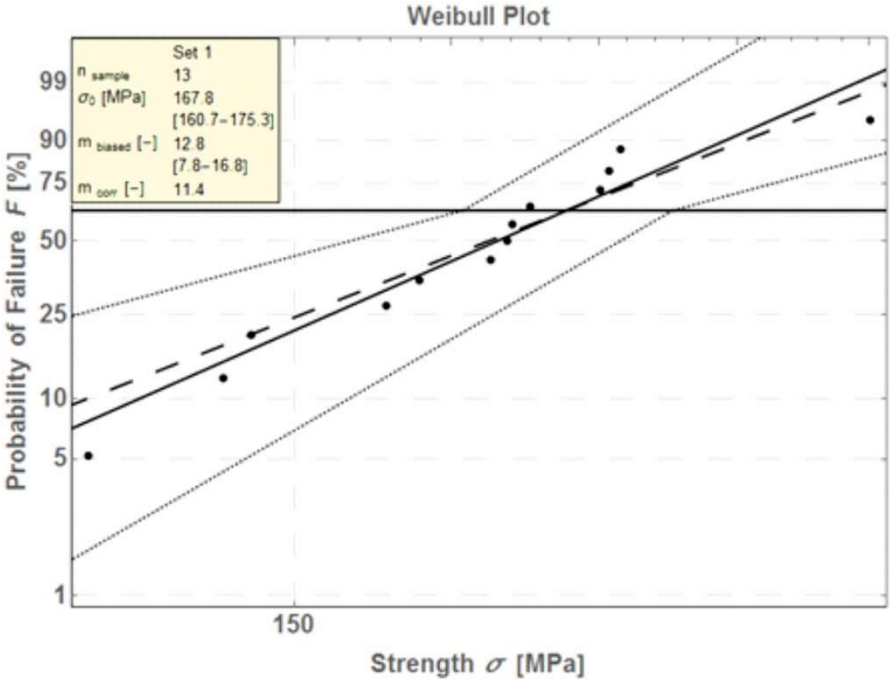

Figure 10: Strength distribution and Weibull parameters of LATP:Si tapes.

Figure 11 shows typical fracture surfaces of LATP:Si in different magnifications. In order to derive the fracture origin, the fracture surfaces of various specimens and individual pieces were analyzed in more detail. As an example, Figures 11 (a) and (b) show the lateral view of the two sides of one individual fracture surface. These images might be interpreted to mean that large grains were removed during fracturing or large individual pores are the crack origin. The critical flaw size was estimated using the following equation [74]:

$$a_c \leq \frac{1}{\pi}\left(\frac{K_{\mathrm{IC}}}{\sigma_0}\right)^2 \tag{3}$$

where K_{R} is the crack growth resistance and σ_0 is the fracture stress. Based on the individual fracture stress of the specimens and the fracture toughness, an a_c of ~ 30 µm was calculated, which is in good agreement with the identified failure origin, which according to Figure 11 (b) had a size of ~ 30 µm. An apparent layer on the sample surface, as visible in the higher magnification shown in Figure 11 (c), was presumed to be the result during exposure to ambient air (formation of lithium carbonates). The small grains were heterogeneously distributed between the large grains and that a number of pores existed both between the grains and inside the large grains. In the case of the small grains, the crack propagated along the grain boundary. As for the larger grains, the crack propagated intergrannually. As shown in Figure 11 (d), the crack went through the internal pores of the grain. Overall, the cracks propagated both intergranularly and transgranularly. This suggests that

the pores weaken the large grains, leading to a lower strength within large grains than that along grain boundaries. Therefore, improving the density of the LATP:Si and LATP microstructure can enhance the material's strength in real application.

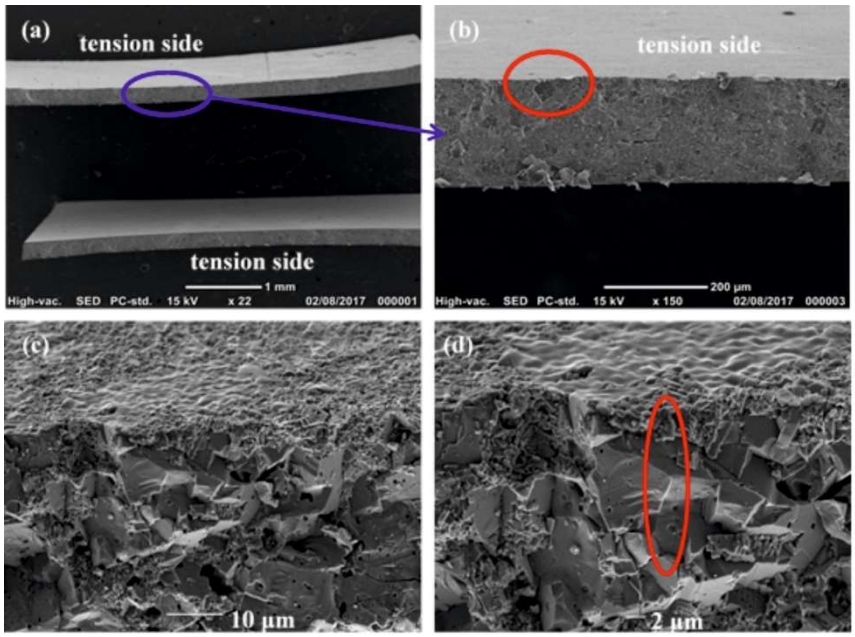

Figure 11: Typical crack surface of an LATP:Si sample. (a), (b), (c) and (d) show the same sample in different magnifications. The blue circle in (a) is shown in enlarged form in (b), where the red circle indicates the potential fracture origin. (c) and (d) show the fracture surface in higher magnifications; in (d), the red circle indicates the transgranular crack growth.

Summary and Conclusions

LATP tapes for applications in all-solid-state Li batteries were produced here by tape casting followed by appropriate thermal treatment. The ionic conductivity and density of the tapes are summarized in Table 3.

Table 3: Total ionic conductivities (σ_{total}) and densities ($\rho_{rel.}$) of LATP sintered at different temperatures and of LATP:Si sintered at 920 °C.

	T_{sinter} / °C	σ_{total} / mS cm^{-1}	$\rho_{rel.}$ / %
LATP	1000	0.30	86.7
	970	0.20	90.8
	950	0.15	92.9
	920	0.10	95.3
	850	0.05	92.7
LATP:Si	920	0.20	99.8

For pure LATP tapes, the highest density was achieved at a sintering temperature of 920 °C. At lower temperatures, sintering was incomplete, while at higher temperatures, grains grew rapidly, leading to

significant intragranular porosity. In contrast, despite the increasing (closed) porosity and the expected increasing number of microcracks, conductivity increased with increasing sintering temperature. These two adverse trends seem to be overcompensated by the reduced number of grain boundaries associated with larger grains because grain boundaries dominate the ionic conductivity. The sintering behavior as well as conductivity can be improved by adding 1.5 % amorphous silica to the tape casting slurry. The resulting LATP:Si sheets are almost fully dense, do not contain crystalline impurity phases, and show doubled ionic conductivity compared to the densest unmodified LATP foil.

The high density of LATP:Si allows reliable investigation of the mechanical properties. This material shows higher elastic modulus and hardness than reported for other LATP materials [31].

The fracture strength as well as Weibull modulus of LATP:Si reported here can provide the basis for future macroscopic modeling of LATP components in solid-state batteries and might be used as indicators for the design of such batteries in terms of safety issues. The observation of the fracture surfaces of LATP:Si revealed that the pores inside large grains or the large grains themselves reduce fracture stresses. The mechanical measurements of LATP:Si demonstrate the improvement of the mechanical properties that can be achieved by densifying the structure and reducing the grain size. Further improvements can be expected with a more homogeneous grain size distribution and minimized porosity after the sintering process.

Acknowledgements

We are grateful to Mrs. H. Moitroux for taking pictures of the samples for the graphical abstract. The authors would like to thank Ms. T. Osipova, Dr. E. Wessel, Ms. J. Nonemacher, Dr. Y. Zou, and Mr. R. Silva from IEK-2, Forschungszentrum Jülich, for their support in terms of microstructural characterization, mechanical testing and fruitful discussions. Gang Yan thanks the support from the China Scholarship Council (CSC) of China. Part of this work was compiled in the project “BenchBATT” (reference no) and funded by the German Federal Ministry of Education and Research (BMBF) under support code 03XP0047B. The authors take responsibility for the content of this publication.

References

[1] Y. Seino, T. Ota, K. Takada, A. Hayashi, M. Tatsumisago, Energy Environ. Sci. 7 (2014) 627-631
[2] I. Svare, F. Borsa, D. R. Torgeson, S. W. Martin, Phys. Rev. B 48 (1993) 9336-9344
[3] N. Kamaya, K. Homma, Y. Yamakawa, M. Hirayama, R. Kanno, M. Yonemura, T. Kamiyama, Y. Kato,S. Hama, K. Kawamoto, A. Mitsui, Nature Mater. 10 (2011) 682-686
[4] P. Bron, S. Dehnen, B. Roling, J. Power Sources 329 (2016) 530-535
[5] Y. Kato, S. Hori, T. Saito, K. Suzuki, M. Hirayama, A. Mitsui, M. Yonemura, H. Iba, R. Kanno, Nature Energy 1 (2016) 16030
[6] H.-J. Deiseroth, S.-T. Kong, H. Eckert, J. Vannahme, Ch. Reiner, T. Zaiß, M. Schlosser, Angew. Chem. Int. Ed. 2008, 47, 755-758
[7] R. P. Rao, N. Sharma, V.K. Peterson, S. Adams, Solid State Ionics 230 (2013) 72-76
[8] V. Epp,O. Gün, H. J. Deiseroth, M. Wilkening, J. Phys. Chem. Lett. 4 (2013) 2118-2123
[9] A. Hayashi, K. Noi, N. Tanibata, M. Nagao, M. Tatsumisago, J. Power Sources 258 (2014) 420-423
[10] M. Duchardt, U. Ruschewitz, S. Adams, S. Dehnen, B. Roling, Angew. Chem. Int. Ed. 57 (2018) 1351-1355
[11] S. Song, H. M. Duong, A. M. Korsunsky, N. Hu, L. Lu, Sci. Rep. 6 (2016) 32330
[12] Q. Ma, M. Guin, S. Naqash, C.-L. Tsai, F. Tietz, O. Guillon, Chem. Mater. 28 (2016) 4821-4828
[13] H. Aono, N. Imanaka, G. Adachi, Acc. Chem. Res. 27 (1994) 265-270
[14] X. Xu, Z. Wen, J. Wu, X. Yang, Solid State Ionics 178 (2007) 29-34
[15] H. Kawai, J. Kuwano, J. Electrochem. Soc. 141 (1994) L78-L79
[16] S. Stramare, V. Thangadurai, W. Weppner, Chem. Mater. 15 (2003) 3974-3990
[17] R. Murugan, V. Thangadurai, W. Weppner, Angew. Chem. Int. Ed. 46 (2007) 7778-7781
[18] V. Thangadurai, S. Narayanan, D. Pinzaru, Chem. Soc. Rev., 43 (2014) 4714-4727
[19] J. S. Thokchom, N. Gupta, B. Kumar, J. Electrochem. Soc. 155 (2008) A915-A920
[20] B. Kumar, D. Thomas, J. Kumar, J. Electrochem. Soc. 156 (2009) A506-A513
[21] E. Yi, W. Wang, S. Mohanty, J. Kieffer, R. Tamaki, R. M. Laine, J. Power Sources 269 (2014) 577-588
[22] M. Kotobuki, et. al., RSC Adv. 9 (2019) 11670
[23] R. Jimenez, A. del Campo, M.L. Calzada, J. Sanz, S.D. Kobylianska, S.O. Solopan, A.G. Belous, J. Electrochem. Soc. (2016): 163, A1653-A1659
[24] P. Zhang, H. Wang, Y.-G. Lee, M. Matsui, Y. Takeda, O. Yamamoto, N. Imanishi, J. Electrochem. Soc. 162 (2015) A1265-A1271
[25] L. Puech, C. Cantau, P. Vinatier, G. Toussaint, P. Stevens, J. Power Sources 214 (2012) 330-336
[26] M. Zhang, Z. Huang, J. Cheng, O. Yamamoto, N. Imanishi, B. Chi, J. Pu, J. Li, J. Alloys Comp. 590 (2014) 147-152
[27] M. Zhang, K. Takahashi, I. Uechi, Y. Takeda, O. Yamamoto, D. Im, D.-J. Lee, B. Chi, J. Pu, J. Li, N. Imanishi, J. Power Sources 235 (2013) 117-221
[28] L. Wang, Y. Lu, J-J. Lee, S. Vail, US 9660241B2 US Patent, 23 may, 2017
[29] R. Inada, K. Ishida, M. Tojo, T. Okada, T. Tojo, Y. Sakurai, Ceramic international, 41 (2015) 11126-11142
[30] C. Monroe, J. Newman, *J Electrochem Soc* **152** (2005) (2) A396.
[31] S.D. Jackman, R.A. Cutler, *J Power Sources* **218** (2012) 65.
[32] Y.-H. Choi, J. Wolfenstine, E. Rangasamy, H. Kim, H. Choe, J. Sakamoto, *Journal of Materials Science* **47** (2012) (16) 5970.
[33] J. Wolfenstine, J.L. Allen, J. Sakamoto, D.J. Siegel, H. Choe, *Ionics* (2017) 1.
[34] X.-W. Zhang, Y. Li, S.A. Khan, P.S. Fedkiw, *J Electrochem Soc* **151** (2004) (8) A1257.
[35] L.L. Baranowski, C.M. Heveran, V.L. Ferguson, C.R. Stoldt, *Acs Appl Mater Inter* **8** (2016) (43) 29573.
[36] F. Aguesse, W. Manalastas, L. Buannic, J.M. Lopez del Amo, G. Singh, A. Llordés, J. Kilner, *Acs Appl Mater Inter* **9** (2017) (4) 3808.
[37] L. Porz, T. Swamy, B.W. Sheldon, D. Rettenwander, T. Frömling, H.L. Thaman, S. Berendts, R. Uecker, W.C. Carter, Y.M. Chiang, *Advanced Energy Materials* **7** (2017) (20).
[38] J.-L. Le, Z.P. Bažant, M.Z. Bazant, *Journal of Physics D: Applied Physics* **42** (2009) (21) 214008.
[39] R. Davidge, J. McLaren, G. Tappin, *Journal of Materials Science* **8** (1973) (12) 1699.
[40] E.C. Teixeira, J.R. Piascik, B.R. Stoner, J.Y. Thompson, *Journal of Materials Science: Materials in Medicine* **18** (2007) (6) 1219.

[41] C. Boissiere, D. Grosso, S. Lepoutre, L. Nicole, A.B. Bruneau, C. Sanchez, *Langmuir* **21** (2005) (26) 12362.
[42] J. Blum, R. Schräpler, *Phys Rev Lett* **93** (2004) (11) 115503.
[43] S. Naqash, Q. Ma, F. Tietz, O. Guillon, Solid State Ionics 302 (2017) 83-91
[44] A. Chanda, B. Huang, J. Malzbender, R. Steinbrech, *J Eur Ceram Soc* **31** (2011) (3) 401.
[45] X. Hu, X. Cheng, S. Qin, G. Yan, J. Malzbender, W. Qiang, B. Huang, *Ceram Int* **44** (2018) (2) 1902.
[46] L.-N. Zhu, B.-S. Xu, H.-D. Wang, C.-B. Wang, *Journal of Materials Science* **47** (2012) (5) 2122.
[47] W.C. Oliver, G.M. Pharr, *J Mater Res* **7** (1992) (6) 1564.
[48] Z. Deng, Z. Wang, I.-H. Chu, J. Luo, S.P. Ong, *J Electrochem Soc* **163** (2016) (2) A67.
[49] F. Sergejev, M. Antonov, *Proc. Estonian Acad. Sci. Eng* **12** (2006) (4) 388.
[50] M. Sebastiani, K. Johanns, E.G. Herbert, G.M. Pharr, *Current Opinion in Solid State and Materials Science* **19** (2015) (6) 324.
[51] G. Anstis, P. Chantikul, B.R. Lawn, D. Marshall, *J Am Ceram Soc* **64** (1981) (9) 533.
[52] A. Börger, P. Supancic, R. Danzer, *J Eur Ceram Soc* **22** (2002) (9-10) 1425.
[53] R. Bermejo, P. Supancic, I. Kraleva, R. Morrell, R. Danzer, *J Eur Ceram Soc* **31** (2011) (5) 745.
[54] S.R. Choi, J.A. Salem and F.A. Holland, NASA Technical Memorandum 107369, (1997)
[55] D. Rettenwander, A. Welzl, S. Pristat, F. Tietz, S. Taibl, G. J. Redhammer, J. Fleig, J. Mater. Chem. A 4 (2016) 1506-1513
[56] http://www.ohara-inc.co.jp/jp/product/electronics/licgc.html.
[57] Y. Iriyama, C. Yada, T. Abe, Z. Ogumi, K. Kikuchi, Electrochem. Commun. 8 (2006) 1287.
[58] C. Yada, Y. Iriyama T. Abe, K. Kikuchi, Z. Ogumi, Electrochem. Commun. 11 (2009) 413.
[59] C. R. Mariappan, M. Gellert, C. Yada, F. Rosciano, B. Roling, Electrochem. Commun. 14 (2012), 25
[60] B. Hirschorn, M.E. Orazem, B. Tribollet, V. Vivier, I. Frateur, M. Musiani, Electrochim. Acta 55 (2010) 6218-6227
[61] H. Aono, E. Sugimoto, Y. Sadaoka, N. Imanaka and G.-y. Adachi, Chem. Lett. 19 (1990) 1825-1828
[62] K. Arbi, S. Mandal, J. M. Rojo, J. Sanz, Chem. Mater. 14 (2002) 1091-1097
[63] M. Kotobuki, M. Koishi, Ceram. Int. 39 (2013) 4645-4649
[64] B. Davaasuren, F. Tietz, Solid State Ionics, 338 (2019) 144-152
[65] E. Dashjav, Q. Ma, Q. Xu, Ch-L. Long, M. Giarola, G. Mariotto, *Solid State Ionics*, 321, 2018, 83–90.
[66] J. Wolfenstine, J. Allen, J. Read, J. Sakamoto, G. Gonalez-Doncel, *J Power Sources* **195** (2010) (13) 4124.
[67] J.E. Ni, E.D. Case, J.S. Sakamoto, E. Rangasamy, J.B. Wolfenstine, *Journal of Materials Science* **47** (2012) (23) 7978.
[68] A.-N. Wang, J.F. Nonemacher, G. Yan, M. Finsterbusch, J. Malzbender, M. Krüger, *J Eur Ceram Soc* (2018).
[69] X. Hu, X. Cheng, S. Qin, G. Yan, J. Malzbender, W. Qiang, B. Huang, *Ceram Int* (2017).
[70] K.G. Schell, F. Lemke, E.C. Bucharsky, A. Hintennach, M. Hoffmann, *Journal of Materials Science* **52** (2017) (4) 2232.
[71] C. ASTM, *West Conshohocken: ASTM International* (2007)
[72] C.B. Carter and M.G. Norton, *Ceramic materials: science and engineering*, Springer Science & Business Media (2007)
[73] M. Gruber, I. Kraleva, P. Supancic, J. Bielen, D. Kiener, R. Bermejo, *J Eur Ceram Soc* **37** (2017) (14) 4397.
[74] C.H. Wang, *Introduction to fracture mechanics*, DSTO Aeronautical and Maritime Research Laboratory Melbourne, Australia (1996)